Results in Engineering 32 (2026) 112525



Contents lists available at ScienceDirect

Results in Engineering

journal homepage: www.sciencedirect.com/journal/results-in-engineering



Research paper

High frequency characterization methodology of the dynamic properties of glass fiber-reinforced thermoplastic composite

David Miñón *, Jon García-Barruetabeña , Beatriz Achiaga

Department of Mechanics, Design and Industrial Management, University of Deusto, Avda. de las Universidades 24, Bilbao, 48902, Bizkaia, Spain

ARTICLE INFO

Keywords:
Composites
Dynamic characterization
Finite element
Thermoplastic
Fiber-reinforced
Viscoelasticity

ABSTRACT

This article presents a experimental-numerical methodology for the high frequency characterization of the dynamic properties of glass fiber-reinforced thermoplastic matrix (GFRTP) composite materials used in automotive applications. Specifically, the homogenized complex modulus of the composite is characterized in a wide frequency range, up to 1500 Hz, using transmissibility functions obtained by seismic excitation. A novel material model which decouples the storage and loss viscoelastic properties and accurately captures the inherent microstructural heterogeneity effects of FRTP composites is presented together with an efficient numerical-experimental procedure based on the Euler-Bernoulli beam and Timoshenko beam finite element formulations. To ensure a reliable parameter identification process, a hybrid optimization strategy combining the Nelder-Mead and particle swarm optimization (PSO) algorithms is successfully implemented. As a result, this approach establishes a robust methodology to accurately predict the high-frequency dynamic response of GFRTP materials directly from experimental transmissibility data.

1. Introduction

In recent years, increasing emphasis has been placed on the development of advanced lightweight materials in the automotive sector that deliver high performance while minimizing environmental impact [1–3]. The use of fiber-reinforced thermoplastic composites (FRTP) in automotive applications is expected to grow due to both environmental regulations promoting recycled content in vehicle components and their advantageous material properties, including high strength-to-weight ratio, fatigue resistance, durability, corrosion resistance, and low density [4,5]. These properties make FRTPs particularly attractive for structural and semi-structural automotive components, where weight reduction contributes to lower fuel consumption and CO2 emissions. At the same time, the increasing electrification of vehicles is shifting Noise, Vibration and Harshness (NVH) challenges towards higher-frequency phenomena, where high frequency structural vibrations become more dominant [6]. Consequently, the accurate characterization of the frequency-dependent dynamic properties of lightweight materials over extended frequency ranges has become increasingly important for predictive vibration analyses and NVH-oriented structural design. However, the dynamic behavior of FRTP materials over these frequency ranges remains insufficiently investigated. This knowledge gap limits the accurate prediction of resonance frequencies, damping capacity, and vibration amplitudes of lightweight structural components under service conditions.

The global demand for fiber-reinforced polymers has nearly tripled over the past decade, increasing from 60 to 170 kilotons [7], and is expected to continue rising in the coming years. This growth has resulted in a significant accumulation of fiber-reinforced composite waste [8,9], emphasizing the urgent need to develop efficient and sustainable recycling solutions. As part of the strategies for minimizing the environmental impact of automotive components, thermoplastic matrices are increasingly employed as alternatives to thermosetting matrices, which have traditionally been used, particularly epoxy, polyester, and acrylic resins [5]. Recycling thermoset composites is particularly challenging due to the presence of permanent crosslinks that characterize the matrix structure, which prevents remelting or remolding, and consequently makes them difficult to recycle [10,11]. Traditional disposal methods for thermoset composites, such as incineration or landfill, are no longer sustainable and are becoming increasingly restricted [12,13]. Unlike thermosetting materials, thermoplastic matrices offer inherent recyclability that thermosets cannot achieve [14]. Thermoplastic composites can be melted and remolded, enabling both matrix and fiber recovery in a single step [15,16], thus facilitating efficient material reuse.

To enable the effective use of FRTP materials in structural applications, their frequency-dependent dynamic properties must be accurately characterized. Although several previous studies have focused on tensile and flexural behavior [17,18], as well as damage resistance [19], fewer efforts have addressed their high-frequency viscoelastic response. This

* Corresponding author.
E-mail addresses: david.minon@deusto.com (D. Miñón), jgarcia.barruetabena@deusto.es (J. García-Barruetabeña), beatriz.achiaga@deusto.es (B. Achiaga).

https://doi.org/10.1016/j.rineng.2026.112525
Received 22 June 2026; Received in revised form 5 August 2026; Accepted 17 August 2026
Available online 19 August 2026
2590-1230/© 2026 The Authors. Published by Elsevier B.V. This is an open access article under the CC BY license (http://creativecommons.org/licenses/by/4.0/).

is particularly important for automotive components such as panels and structural parts, whose in-service performance is strongly affected by noise, comfort, road-induced vibrations, and impacts across a broad frequency spectrum. Fiber-reinforced composites exhibit complex dynamic responses due to their intrinsic heterogeneity and internal shear effects which produce energy loss, as investigated in recent micromechanical studies [20,21], who investigated the influence of processing parameters on the dynamic behavior of polymer-matrix composites. However, the high-frequency dynamic properties of thermoplastic matrix composites remain poorly characterized, highlighting the need to develop a robust methodology to accurately determine their complex modulus, $E^*(\omega)$, across a wide frequency spectrum to ensure structural performance from the design process. The complex modulus can be described as

Fiber-reinforced composites exhibit complex dynamic responses due to their intrinsic heterogeneity and internal shear effects which produce energy loss, as investigated in recent micromechanical studies

$$E^*(\omega) = E'(\omega) + \mathrm{i}E''(\omega) = E'(\omega)\,[1 + \mathrm{i}\,\eta(\omega)], \tag{1}$$

where $E'(\omega)$ and $E''(\omega)$ denote the storage and loss moduli respectively, while the loss factor is expressed as $\eta(\omega) = E''(\omega)/E'(\omega)$.

To empirically characterize the dynamic properties of polymeric and composite materials, particularly their complex modulus, several experimental techniques can be employed depending on the frequency range of interest. These include rheological methods, Dynamic Mechanical Thermal Analysis (DMTA) [22,23], and the ASTM E756-05(2017) standard test method which estimates dynamic properties from resonance frequencies and damping ratios using the half-power bandwidth method. Time-temperature superposition is also commonly used to extend the accessible frequency range by shifting temperature-dependent data [24,25]. In addition, analytical approaches such as the Ross-Kerwin-Ungar (RKU) model [26,27] have been widely applied to estimate damping in laminated composite structures [28]. Although these techniques provide valuable information, they are often limited when the objective is to identify frequency-dependent material properties over a broad high-frequency range from the full dynamic response of heterogeneous thermoplastic composites.

In this context, vibration-based numerical-experimental methodologies offer a suitable framework for identifying the dynamic properties of the composite material, specifically the storage modulus and the loss factor. In previous studies [29], frequency response functions (FRFs) were employed to characterize the dynamic behavior of an automotive laminated glass ceiling using hammer excitation. Furthermore, the fundamentals of the seismic experimental procedure were previously studied in [30], where a material characterization methodology based on ASTM E756 is detailed. Compared with conventional approaches, the proposed numerical-experimental methodology based on seismic excitation allows the complete dynamic response of the specimen to be considered during the identification process. This is particularly relevant for GFRTP composites, whose intrinsic heterogeneity and internal shear mechanisms may produce frequency-dependent stiffness and energy dissipation effects that are difficult to capture using simplified characterization procedures based solely on resonance parameters.

A key aspect for the curve fitting based methodology is the selection of an appropriate GFRTP material model for the complex modulus, $E^*(\omega)$. Classical linear viscoelastic models, such as Maxwell formulations, are widely used to describe frequency-dependent behavior [31]. However, as discussed in Section 4 their parameter structure may impose a strong coupling between the storage modulus and the loss modulus, limiting their ability to independently reproduce stiffness dispersion and damping over a broad frequency range. For this reason, this work considers a novel phenomenological material model specifically aimed at describing the high-frequency dynamic behavior of GFRTP composites, allowing the storage and loss components of the complex modulus to be adjusted with greater flexibility.

The identification of the material properties is carried out through a finite-element-based numerical model of cantilever beams subjected to seismic base excitation. Two one-dimensional beam formulations are considered. The Euler-Bernoulli beam theory provides a simple and computationally efficient formulation, suitable for slender beams and useful as a reference model [32]. The Timoshenko beam theory is also implemented in order to account for transverse shear deformation and rotary inertia, which may become relevant in moderately thick composite beams and at higher frequencies [33,34]. The comparison between both formulations allows the influence of shear effects on the identified dynamic properties to be assessed and provides a numerical framework that can be extended to more complex structural configurations.

The material model parameters are obtained through a numerical optimization procedure combining global and local search strategies. The Nelder-Mead simplex algorithm is used as a local optimization method due to its efficiency in problems where gradients are not readily available [35–37]. However, this method may be sensitive to the initial parameter values and does not guarantee convergence to the global optimum [38,39]. Particle Swarm Optimization (PSO), originally proposed as a population-based stochastic search algorithm [40,41], is employed to improve the exploration of the parameter space and reduce sensitivity to the initial parameter values. The hybrid NM-PSO strategy combines the global exploration capability of PSO with the faster local convergence of Nelder-Mead, a combination that has been shown to improve robustness and efficiency in multimodal and engineering optimization problems [42–44].

This paper therefore presents a methodology for the high-frequency characterization of GFRTP composites using experimental transmissibility functions obtained from cantilever beams subjected to seismic excitation. The proposed approach identifies the frequency-dependent storage modulus and loss factor by fitting finite element simulations to the measured transmissibility functions. As a result, the methodology provides a predictive framework to incorporate the dynamic behavior of GFRTP materials into the design and vibration analysis of automotive structural components. The article is structured as follows: Section 2 describes the experimental setup and the transmissibility functions obtained via seismic excitation. Section 3 presents the numerical procedure, including the Euler-Bernoulli and Timoshenko finite element formulations, the proposed material model, and the parameter identification strategy. Finally, Section 4 compares the numerical and experimental results and discusses the identified high-frequency dynamic properties of the GFRTP specimens.

2. Experimental procedure

This section presents the experimental procedure employed to characterize the dynamic behavior of GFRTP composite using transmissibility functions. First, the GFRTP material description and the geometry of the tested specimens are detailed. Next, the experimental setup, including instrumentation and measurement conditions, is presented. Finally, the dynamic response of the specimens is analyzed by extracting modal parameters from the measured transmissibility function, providing key parameters for subsequent characterization process.

2.1. Specimen description

The specimens tested in this study are rectangular cross-section GFRTP beams extracted from a larger laminate plate. In order to evaluate possible spatial variability in the dynamic properties of the laminate, the specimens were divided into three groups, denoted as G1, G2, and G3. Each group consisted of beam specimens cut from a different region of the plate. The dynamic properties reported for each group therefore correspond to the mean response of the specimens belonging to that group. The base material used is a commercial commingled fabric (Comfil 30028-17), which integrates polypropylene (PP) fibers and E-glass reinforcement. This hybrid fabric features a 2/2 twill weave with a grammage of 700 g/m^2 and a reinforcement content of 60% by weight (equivalent to 34% by volume).

Table 1
Mean cross-sectional dimensions and density of the GFRTP specimen groups.

Group	b (mm)	h (mm)	ρ (kg/m^3)
G1	10.34 ± 0.1	2.06 ± 0.01	1322.08 ± 0.02
G2	10.24 ± 0.1	2.08 ± 0.01	1301.27 ± 0.02
G3	10.37 ± 0.1	2.09 ± 0.01	1276.28 ± 0.02

The final laminates consist of a stacking sequence of four layers of the commingled fabric and three layers of a compatibilizing veil integrated at the interfaces to ensure interlaminar integrity. The material was consolidated using a double-belt laminator operating at a constant temperature of 250 °C, a pressure of 2 bar, and a feed speed of 0.5 m/min. The final consolidated thickness was achieved after two passes through the laminator.

The mean dimensions and physical properties of the GFRTP specimen groups are detailed in Table 1, where h denotes the thickness, b the width, and ρ the density.

2.2. Experimental setup

The experimental procedure was based on ASTM E756-05(2017), which specifies the use of non-contact transducers to apply an excitation force to a cantilever specimen and obtain its frequency response function. In the present study, however, seismic excitation was applied to cantilever-beam-like specimens in order to obtain the transmissibility function as it provides a uniform and minimally intrusive excitation, which is particularly suitable for lightweight or low-stiffness composite structures, while avoiding the variability and potential damage associated with impact testing. Transmissibility functions were obtained with one end of the beam clamped and the other end free, resulting in a cantilever length (L) of 90 mm. The measurement point was located 5 mm from the free end of the specimen, a location that ensures high modal amplitudes and a high signal-to-noise ratio across the analyzed frequency spectrum. A schematic of the experimental setup is shown in Fig. 1.

The applied base acceleration was white noise in the frequency range from 40 to 1500 Hz, generated by an LDS 406 electrodynamic shaker. This frequency range provided a sufficiently stable excitation level and measured response, representative of the specimen dynamics. The lower frequency limit of 40 Hz was selected to ensure reliable dynamic excitation and measurement conditions, as very low-frequency operation may reduce shaker efficiency and compromise the signal-to-noise ratio. A mean power spectral density (PSD) value of $0.001\,(\mathrm{m}\cdot\mathrm{s}^2)^2/\mathrm{Hz}$ was selected as a measure of the power distribution of the signal across the frequency spectrum, under which the specimen exhibited a linear response over the entire measured frequency range. PSD value was measured using a Brüel and Kjaer (B&K) triaxial accelerometer, connected to a LAN XI input module, also from B&K, and controlled via LASER USB 2.0. All measurements were performed at room temperature. The response at the measurement points of the cantilevered beams was acquired in the shaker base motion direction using a Polytec PDV 100 laser vibrometer. Data acquisition and frequency-domain signal processing were conducted using BK Connect software and transmissibility functions ($\mathrm{m}\cdot\mathrm{s}^{-2}/\mathrm{m}\cdot\mathrm{s}^{-2}$) were computed. The frequency resolution of the measurements was 0.31 Hz.

2.3. Experimental results

The dynamic response of the GFRTP specimens was characterized by analyzing the complex transmissibility functions, $T^*_{i,\mathrm{exp}}(\omega)$, which relates the response signal to the acceleration at the shaker base, obtained from the different specimen groups. The subscript i denotes the index of the measured point, ω is the angular frequency and an asterisk is used to identify complex-valued quantities. The resulting functions are shown in Fig. 2 for the three tested specimen groups. The experimental data reveal a consistent dynamic behavior across the 40-1500 Hz range, characterized by two primary resonance peaks associated with the first and second bending modes of the structure.

Table 2
Modal parameters for the first and second resonances of the tested specimen groups.

	Resonance	Frequency f (Hz)	Amplitude A ($\mathrm{m\,s^{-2}/m\,s^{-2}}$)	Damping ratio ξ
G1	First	109.4	79.7	0.0114
	Second	690.0	22.0	0.0156
G2	First	110.0	81.6	0.0099
	Second	700.6	23.9	0.0129
G3	First	110.6	89.2	0.0099
	Second	710.0	30.1	0.0112

Table 2 presents the mean modal parameters, resonance frequencies, peak amplitudes, and damping ratios, derived directly from the individual T^* functions for each specimen group. Although the low variability observed between groups confirms the high repeatability of the manufacturing and testing procedures, slight differences in the modal parameters can still be identified. Differences arising from the specific geometry of each specimen are not expected to bias the proposed numerical methodology, since the measured dimensions of each sample are explicitly incorporated into the corresponding finite element model. In contrast, variations associated with the material composition or microstructural heterogeneity across the original laminate plate, which have been shown to influence identified material parameters [20], are reflected in the dynamic characterization of each group. These group-averaged experimental transmissibility functions are therefore used as target responses in the subsequent numerical optimization process to identify the homogenized complex modulus of the GFRTP material.

3. Numerical procedure

This section presents the numerical modeling via the Finite Element Method (FEM) for the seismic excitation of the GFRTP cantilevered beams. First, the governing equation of structural dynamics, its boundary conditions and the material model for the complex modulus of the GFRTP are introduced. Then, two different one-dimensional finite element approaches of the physical problem for the transmissibility function calculation are presented. On the one hand, the Euler-Bernoulli beam theory, which represents a simple and easily implementable approach in most programming languages. On the other hand, the Timoshenko beam theory, which accounts for transverse shear deformation in moderately thick beams. Finally, the identification of the material model parameters was carried out through a numerical-experimental curve fitting procedure based on Nelder-Mead and PSO optimization algorithms, using the transmissibility function as the target response.

3.1. Problem modelling

Structural dynamic behavior is governed by the following equation of motion:

$$\mathbf{M}\,\ddot{\mathbf{u}}(t) + \mathbf{K}^*\mathbf{u}(t) = \mathbf{f}(t), \tag{2}$$

where the mass matrix, complex stiffness matrix, and force vector are denoted by $\mathbf{M}$, $\mathbf{K}^*$, and $\mathbf{f}(t)$, respectively. Two finite element beam formulations were considered to model the seismic excitation: the Euler-Bernoulli theory for thin beams and the Timoshenko theory to account for shear deformation and rotary inertia. Both approaches employ a two-node discretization with transverse displacement and rotation as nodal degrees of freedom. The detailed mass and stiffness matrices for both formulations, including the auxiliary shear parameters for the Timoshenko model, are provided in Appendix A.

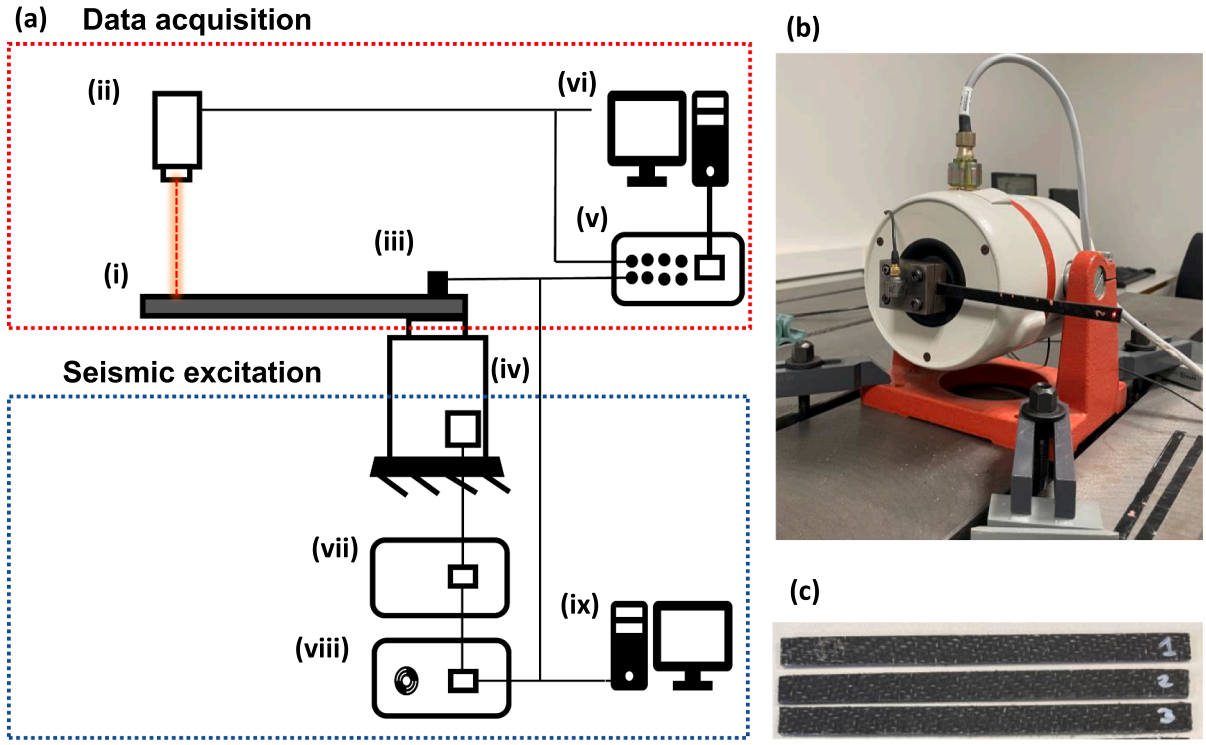

Fig. 1. Experimental setup for seismic excitation of the GFRTP beam: (a) test setup including (i) GFRTP specimen, (ii) laser vibrometer, (iii) accelerometer, (iv) LDS 406 electrodynamic shaker, (v) LAN-XI data acquisition hardware, (vi) computer for data acquisition, (vii) laser signal amplifier, (viii) LASER USB 2.0 vibration controller, and (ix) computer for vibration control; (b) seismic excitation of the beam; and (c) GFRTP specimens from different tested groups.

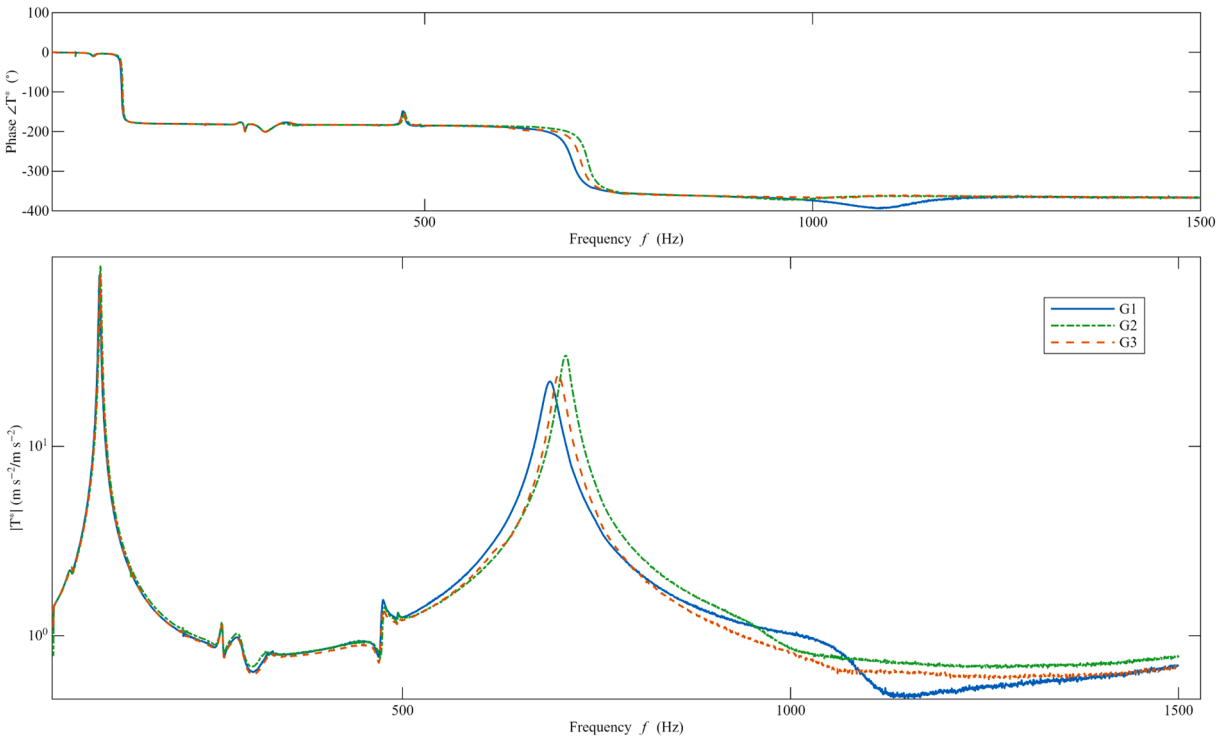

Fig. 2. Experimental complex transmissibility functions (T^*) for the GFRTP specimen groups recorded at 5 mm from the free end of the cantilever beam. The figure displays the dynamic response of each group in three different colors across the 40-1500 Hz frequency range. The upper subplot shows the phase response $\angle T^*$, while the lower subplot illustrates the magnitude $|T^*|$ on a logarithmic scale.

Table 3
Comparison of relative errors (%) for modal parameters: Maxwell and phenomenological material model T^* vs. experimental T^*_{exp}.

	Modal Parameter	Maxwell Error (%)	Phen. Error (%)
First Resonance	Frequency f (Hz)	+2.62	+0.29
	Amplitude A (m·s^{-2}/m·s^{-2})	−7.63	−7.63
	Damping ratio ξ	+14.62	+11.36
Second Resonance	Frequency f (Hz)	−0.18	−0.05
	Amplitude A (m·s^{-2}/m·s^{-2})	−25.30	−0.68
	Damping ratio ξ	+38.35	+3.22

To account for the seismic excitation within the numerical scheme, the total displacement vector is partitioned into restrained and free degrees of freedom as $\mathbf{u}(t) = \{\mathbf{u}_1(t)\ \mathbf{u}_2(t)\}^T$. Here, $\mathbf{u}_1(t)$ represents the prescribed base motion vector, whereas $\mathbf{u}_2(t)$ encompasses the remaining unknown degrees of freedom. Consequently, Eq. (2) can be recast as

$$\begin{bmatrix}\mathbf{M}_{11} & \mathbf{M}_{12}\\ \mathbf{M}_{21} & \mathbf{M}_{22}\end{bmatrix}\begin{bmatrix}\ddot{\mathbf{u}}_1(t)\\ \ddot{\mathbf{u}}_2(t)\end{bmatrix} + \begin{bmatrix}\mathbf{K}^*_{11} & \mathbf{K}^*_{12}\\ \mathbf{K}^*_{21} & \mathbf{K}^*_{22}\end{bmatrix}\begin{bmatrix}\mathbf{u}_1(t)\\ \mathbf{u}_2(t)\end{bmatrix} = \begin{bmatrix}\mathbf{f}_1(t)\\ 0\end{bmatrix}, \tag{3}$$

where $\mathbf{f}_1(t)$ contains the reaction forces. By retaining only the equations corresponding to the free degrees of freedom, the reduced system is obtained as

$$\mathbf{M}_{22}\,\ddot{\mathbf{u}}_2(t) + \mathbf{K}^*_{22}\,\mathbf{u}_2(t) = -\,\mathbf{M}_{21}\,\ddot{\mathbf{u}}_1(t) - \mathbf{K}^*_{21}\,\mathbf{u}_1(t), \tag{4}$$

where the right-hand side denotes the equivalent forces induced by the ground motion at the base. Transforming Eq. (4) into the frequency domain via the Fourier transform leads to

$$\left[-\omega^2\mathbf{M}_{22} + \mathbf{K}^*_{22}\right]\mathbf{U}^*_2 = \left[\omega^2\mathbf{M}_{21} - \mathbf{K}^*_{21}\right]\mathbf{U}^*_1, \tag{5}$$

thus, the transmissibility matrix is computed as

$$\mathbf{T}^*_{\text{num}}(\omega) = \left[-\omega^2\mathbf{M}_{22} + \mathbf{K}^*_{22}\right]^{-1}\left[\omega^2\mathbf{M}_{21} - \mathbf{K}^*_{21}\right]. \tag{6}$$

The complex dynamic behaviour of the beam structure is modelled through the complex stiffness matrix defined as $\mathbf{K}^*(\omega) = \mathbf{K}_0(E^*/E_{ini})$. In this equation, $\mathbf{K}_0$ is the static stiffness at $\omega = 0$, in which an initial constant modulus E_{ini} is considered. For the complex modulus of GFRTP $E^*(\omega)$, which introduces the structural damping, the following viscoelastic material model [45] is proposed,

$$E^*(\omega) = E_0 + \Delta E\,(1 - e^{-\mu\omega}) + \mathrm{i}2c\omega e^{-t_0\omega}, \tag{7}$$

where E_0, μ, c and t_0 are parameters of the model. The complex modulus is decomposed into its real and imaginary components, which dictate the storage modulus $E'(\omega)$ and the loss modulus $E''(\omega)$, respectively. E_0 is the relaxed modulus, corresponding to the value of the storage modulus at $\omega = 0$; c is the viscous constant; μ and t_0 are the time decay constants of the storage and loss moduli, respectively. The loss factor $\eta(\omega)$ is derived as:

$$\eta(\omega) = \frac{2c\omega e^{-t_0\omega}}{E_0 + \Delta E(1 - e^{-\mu\omega})}, \tag{8}$$

where $t_0 > \mu$. This formulation provides a significant advantage in mathematical flexibility for describing the energy dissipation behavior of GFRTP specimens compared to traditional viscoelastic models. The modal parameter identification results, supported by the comparative analysis in Fig. 3, demonstrate that the proposed phenomenological material model reproduces the experimental transmissibility curves with significantly higher fidelity than a classical single-branch Maxwell model. As illustrated in the detailed views of the first and second resonances (Fig. 3, right panels), the Maxwell model (blue dashed line) consistently underestimates the resonance amplitudes and fails to capture the precise width of the peaks, leading to substantial errors in damping estimation.

The observed discrepancy in fitting accuracy arises from the inherent parameter coupling found in the Maxwell formulation. In a single-branch Maxwell model, the stiffness dispersion, the loss peak amplitude, and the characteristic frequency are governed by only two parameters: E_1 and τ_1. Consequently, the model cannot adjust the storage modulus increment independently of the damping peak height. In contrast, the proposed model (Eq. (7)) decouples these effects; the parameter c serves as the primary controller for the loss modulus amplitude, while t_0 independently determines the peak's spectral position and decay rate. As quantified in Table 3, this additional flexibility allows the numerical procedure to capture the specific viscoelastic trends of GFRTP specimens precisely.

3.2. Numerical-experimental fitting

The identification of the optimal material model parameters $\mathbf{p} = [E_0, \Delta E, \mu, c, t_0]$ was performed by minimizing a multi-objective function that quantifies the discrepancy between the experimental T^*_{exp} and the numerical T^*_{num}. To ensure a robust identification process and overcome the non-convex nature of the error surface, a hybrid optimization strategy was employed. This approach combines the Nelder-Mead simplex algorithm, as implemented in the fminsearchbnd function of MATLAB, for efficient local convergence with Particle Swarm Optimization (PSO) to explore the global parameter space. In this hybrid scheme, PSO reduces the risk of the optimization becoming trapped in local minima, while Nelder-Mead accelerates convergence once the search has approached a promising region of the parameter space. This combined use significantly enhances the optimization performance in terms of accuracy and computational efficiency. The objective function, $J(\mathbf{p})$, is defined as a weighted sum of three distinct error components, targeting the most physically significant features of the dynamic response:

$$J(\mathbf{p}) = \alpha \cdot err_{freq} + \beta \cdot err_{amp} + \gamma \cdot err_{phase} \tag{9}$$

where α, β, and γ are the relative weighting factors assigned to frequency, amplitude, and phase, respectively. Their specific values, further justified in Section 4, were selected to normalize the disparate orders of magnitude of the residuals, ensuring a balanced optimization process.

- Frequency error (err_{freq}): This term calculates the relative difference between the identified numerical and experimental resonance frequencies for the first two modes. Since the locations of resonance peaks are fundamentally defined by the storage modulus, this term is the primary driver for identifying E_0 and μ.
- Amplitude error (err_{amp}): This component measures the normalized difference between the peak amplitudes. Since the peak height in the transmissibility function is inversely related to energy dissipation, this term is critical for the accurate identification of the loss factor parameters (c, t_0).
- Phase error (err_{phase}): To ensure global consistency, the unwrapped phase difference is minimized. This error is modulated by a normalized weight function, $w(\omega)$, which is defined as the sum of two Gaussian functions centered at the experimental resonances. Following the experimental procedure, the phase error is computed as:

$$err_{phase} = \frac{\| w(\omega)\cdot(\phi_{num} - \phi_{exp}) \|}{\| w(\omega)\cdot\phi_{exp} \|} \tag{10}$$

where ϕ_{num} and ϕ_{exp} represent the numerical and experimental unwrapped phase, respectively. The standard deviations ($\sigma_1 = 20$ Hz, $\sigma_2 = 50$ Hz) were selected to prioritize frequency bands with the highest signal-to-noise ratio, ensuring that the optimization emphasizes the spectral regions that most accurately reflect the material's viscoelastic behavior.

3.3. Analytical validation

The analytical validation of the numerical methodology is essential to ensure the reliability of the finite element procedure before its application to more complex structural problems where analytical solutions

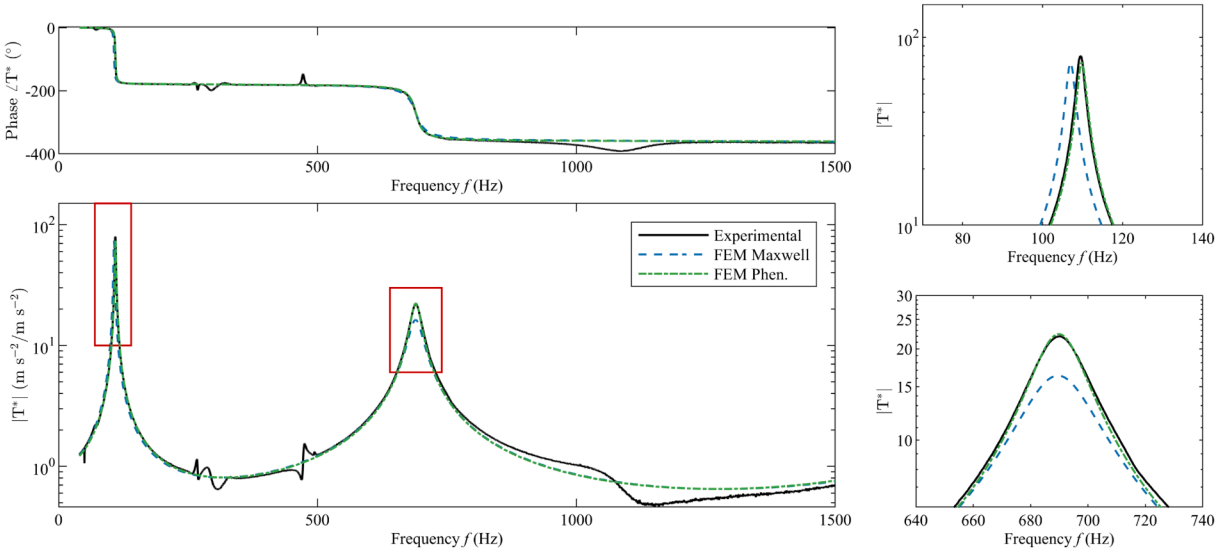

Fig. 3. Comparison of experimental transmissibility function with numerical FE fits obtained from the classical single-branch Maxwell material model and the proposed phenomenological material model. The main panel displays the full frequency spectrum, modulus and phase, while the right-hand insets provide detailed views of the first (top) and second (bottom) resonance peaks. In solid black, the experimental transmissibility; in dashed blue, single-branch Maxwell model numerical fitting; and in dash-dotted green, the proposed phenomenological model numerical fitting. (For interpretation of the references to colour in this figure legend, the reader is referred to the web version of this article.)

are unavailable. For instance, while the Euler-Bernoulli (EB) theory provides a well-known analytical benchmark for thin beams, extending the methodology to the Timoshenko beam theory or two-dimensional plate models requires a robust numerical framework. The analytical transmissibility function $T_{\mathrm{AN}}(x,\omega)$ for a cantilever beam is derived from the EB governing equations by imposing unit transmissibility at the base (x = 0). The general solution is expressed as:

$$T^*_{\mathrm{AN}}(x,\omega) = A^*\sinh(qx) + B^*\cosh(qx) + C^*\sin(qx) + D^*\cos(qx),$$

$$\begin{cases} A^* = \dfrac{1+\cos(q^*L)\cosh(q^*L)-\sin(q^*L)\sinh(q^*L)}{2(1+\cos(q^*L)\cosh(q^*L))}, \\ B^* = \dfrac{\cos(q^*L)\sinh(q^*L)+\sin(q^*L)\cosh(q^*L)}{2(1+\cos(q^*L)\cosh(q^*L))}, \\ C^* = -A^*, \\ D^* = 1-B^*. \end{cases} \tag{11}$$

where $q^*(\omega) = (\omega^2\rho A/E^*(\omega)I)^{1/4}$ denotes the complex wave number, and the coefficients A, B, C, D are determined via the boundary conditions. Specifically, these conditions demand unit transmissibility along with a zero slope at the clamped boundary ($x = 0$), alongside a vanishing bending moment and shear force at the free termination ($x = L$). The resonance frequencies are identified when the denominator of these coefficients tends to zero, which fulfills the characteristic transcendental equation $\cos(qL)\cosh(qL) = -1$. To evaluate the accuracy of the 1D finite element implementation, a mesh convergence analysis was performed by comparing the numerical transmissibility (T_{FEM}) with the analytical solution T_{AN}. Four different mesh densities consisting of 9, 18, 36, and 72 elements were evaluated. The error was quantified using the L_2 norm across the entire measured frequency range (40–1500 Hz). As shown in Table 4, the numerical solution demonstrates an excellent convergence rate, with the error decreasing significantly as the mesh is refined.

The resulting log-log plot of the error versus element number (Fig. 4) confirms the robustness and high convergence rate of the numerical procedure. Furthermore, a detailed view of the resonance peaks (Fig. 5) reveals that, consistent with theoretical expectations, the identified parameters for the Timoshenko model show a slight shift in modal frequen-

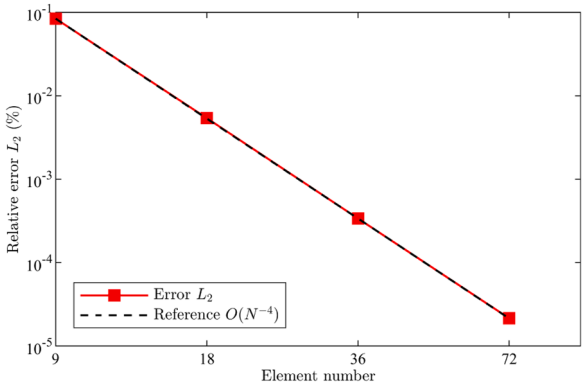

Fig. 4. Numerical convergence analysis. The red curve shows the log-log plot of the L_2 norm error versus the number of elements, while the dashed black line indicates fourth-order convergence. (For interpretation of the references to colour in this figure legend, the reader is referred to the web version of this article.)

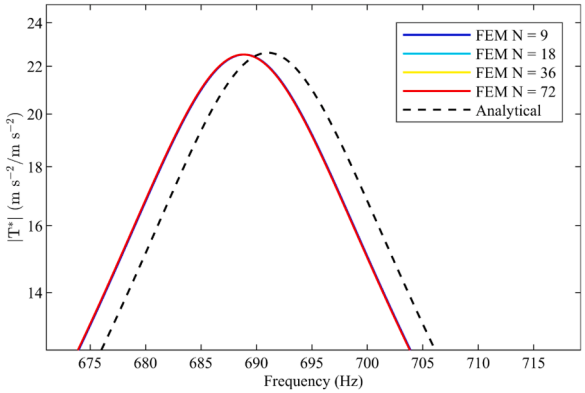

Fig. 5. Timoshenko finite element model results, T_{FEM}, for different element number, compared with the analytical Euler-Bernoulli solution, T_{AN}, shown as a dashed black line.

Table 4
Convergence of the FE model relative to the analytical EB solution.

Number of Elements	L_2 Norm Error	Convergence Order
9	0.086385	–
18	0.005545	3.9616
36	0.000348	3.9938
72	0.000022	3.9727

cies compared to the EB analytical solution. This discrepancy further justifies the use of the Timoshenko FE approach in the GFRTP specimens tested in this study.

4. Result comparison and discussion

The dynamic response of GFRTP specimens was characterized using experimental transmissibility functions derived from seismic base excitation. The homogenized complex modulus was identified by fitting the proposed phenomenological model (Eq. (10)) to the experimental data using a hybrid optimization strategy.

The suitability of the material model was evaluated through a quantitative comparison against the classical single-branch Maxwell model, as summarized in Table 3. While both formulations provide reasonable estimates for the first resonance frequency, the performance of the Maxwell model degrades significantly at higher frequencies. Specifically, for the second resonance mode, the Maxwell model exhibits a substantial and unacceptable relative error of -25.30% in vibration amplitude and +38.35% in the damping ratio (ξ). This critical discrepancy stems from the inherent parameter coupling within the Maxwell formulation. In a single-branch Maxwell model,

$$E^* = E_0 + E_1 \frac{i\omega\tau_1}{1 + i\omega\tau_1}, \tag{12}$$

the storage modulus dispersion and the damping peak height are rigidly linked by only two parameters (E_1 and τ_1), which effectively fixes the maximum loss modulus at $E''_{\max} = E_1/2$ at the frequency $\omega = 1/\tau_1$. This structural rigidity prevents the model from independently adjusting the stiffness increment relative to the energy dissipation height. As illustrated in the detailed insets of Fig. 3, this leads to a consistent underestimation of resonance amplitudes and a failure to capture the precise spectral width of the peaks. In contrast, the proposed phenomenological model (Eq. (7)) overcomes these limitations by decoupling the storage and loss effects. This mathematical flexibility allows the parameter c to act as the primary controller for the loss modulus amplitude, while t_0 independently determines the peak's spectral position and decay rate. Consequently, the numerical procedure achieves a high-fidelity fit, reducing errors in the second resonance to just -0.68% in amplitude and +3.22% in the damping ratio. This independent control over the complex modulus components is essential for accurately reproducing the frequency-dependent dynamic behavior of GFRTP specimens across the entire 40–1500 Hz range. However, it should be noted that this phenomenological approach is intended for high-fidelity fitting within the 40–1500 Hz range. While the model yields excellent agreement with the experimental data, physical causality in linear viscoelasticity requires the storage and loss moduli to satisfy the Kramers-Kronig relations [46,47]. Since the parameters in Eq. (7) are optimized to accurately reproduce the experimental response within the measured frequency range without explicitly enforcing this constitutive coupling, caution should be exercised when extrapolating the material behavior beyond the bandwidth. This is particularly relevant for extrapolations towards very low frequencies, where the absence of causality constraints may lead to physically inconsistent predictions. Nevertheless, the proposed model provides an accurate, robust and computationally efficient representation of the complex modulus of GFRTP, making it well suited for predictive dynamic analyses in this frequency range.

The optimized parameters of the phenomenological model are summarized in Table 5 for specimen groups G1, G2, and G3. The table also reports the final value of the objective function, $J(\mathbf{p})$, and compares the results obtained using the EB and Timoshenko beam theories. To ensure a balanced contribution of each residual term within the multi-objective function, specific weighting factors were introduced: $\alpha = 10$, $\beta = 0.1$, and $\gamma = 1$. This weighting scheme compensates for the different orders of magnitude of the frequency, amplitude, and phase residuals. Without such scaling, the optimization would be numerically dominated by the amplitude error, whose initial values are approximately one order of magnitude larger than those associated with the frequency and phase terms. The adopted weighting factors therefore normalize the residual contributions, preventing the optimizer from focusing predominantly on a single response feature. A sensitivity analysis was also performed by varying the weighting factors within a ±20% range. The identified material parameters remained stable and consistent, confirming the robustness of the optimization procedure with respect to the specific choice of weights.

The identified dynamic properties for the GFRTP specimen groups, specifically the storage modulus (E') and loss factor (η), are illustrated in Fig. 6. A clear viscoelastic trend is observed across the analyzed frequency range for all GFRTP specimen groups: the storage modulus exhibits a gradual increase with frequency. The loss factor curves reach a distinct peak, identifying the frequency of maximum energy dissipation. For the groups evaluated, the EB model identifies this dissipation peak at approximately 395 ± 3 Hz, while the Timoshenko formulation, which accounts for transverse shear deformation and rotary inertia, yields a practically identical value of approximately 395 ± 4 Hz. These results indicate that the frequency of maximum energy dissipation remains highly consistent among the different specimen groups and is not significantly affected by the adopted beam formulation. To further quantify the influence of the beam theory, the percentage differences between the material properties identified using the Euler-Bernoulli and Timoshenko models were evaluated over the entire experimental frequency range (40-1500 Hz). For all specimen groups, the maximum difference in the storage modulus remained below 1.3%, whereas the maximum difference in the loss factor did not exceed 3.8%. These results confirm that, despite the inclusion of transverse shear deformation and rotary inertia in the Timoshenko formulation, both beam theories provide very similar frequency-dependent material properties for the relatively slender specimens considered ($L/h \approx 43.7$).

The high fidelity of the proposed phenomenological model is further evidenced in Fig. 7, which compares the numerical transmissibility functions against experimental data. The model accurately reproduces the dynamic response across the entire spectrum, capturing both the first and second bending modes with high precision. To quantitatively evaluate the methodology's performance, Table 6 summarizes the percentage errors for frequency, amplitude, and damping ratio. The results demonstrate remarkable accuracy in identifying resonance locations, with frequency errors for the first mode ranging from 0.00% to 1.14% across all specimens. Although a consistent amplitude error of approximately -7.6% is observed for the first mode, the overall stability of the errors across different specimens confirms the robustness of the hybrid optimization strategy. These results indicate that the one-dimensional finite element approach provides a reliable and computationally efficient framework for characterizing the high-frequency dynamic behavior of GFRTP specimens.

Table 5
Identified material parameters for each specimen group and finite element scheme.

	FEM	E_0 (GPa)	ΔE (GPa)	μ (10^{-5} s)	c (10^5 Pa s)	t_0 (10^{-4} s)	$J(\mathbf{p})$
G1	EB	8.58	1.99	1.26	1.61	4.04	0.39
	Tim.	8.69	0.84	1.22	1.62	4.01	0.41
G2	EB	8.89	2.82	0.62	1.60	4.03	0.44
	Tim.	9.00	0.83	0.36	1.61	4.00	0.46
G3	EB	8.94	0.70	10.00	1.48	4.05	0.30
	Tim.	8.94	0.97	8.70	1.48	4.01	0.31

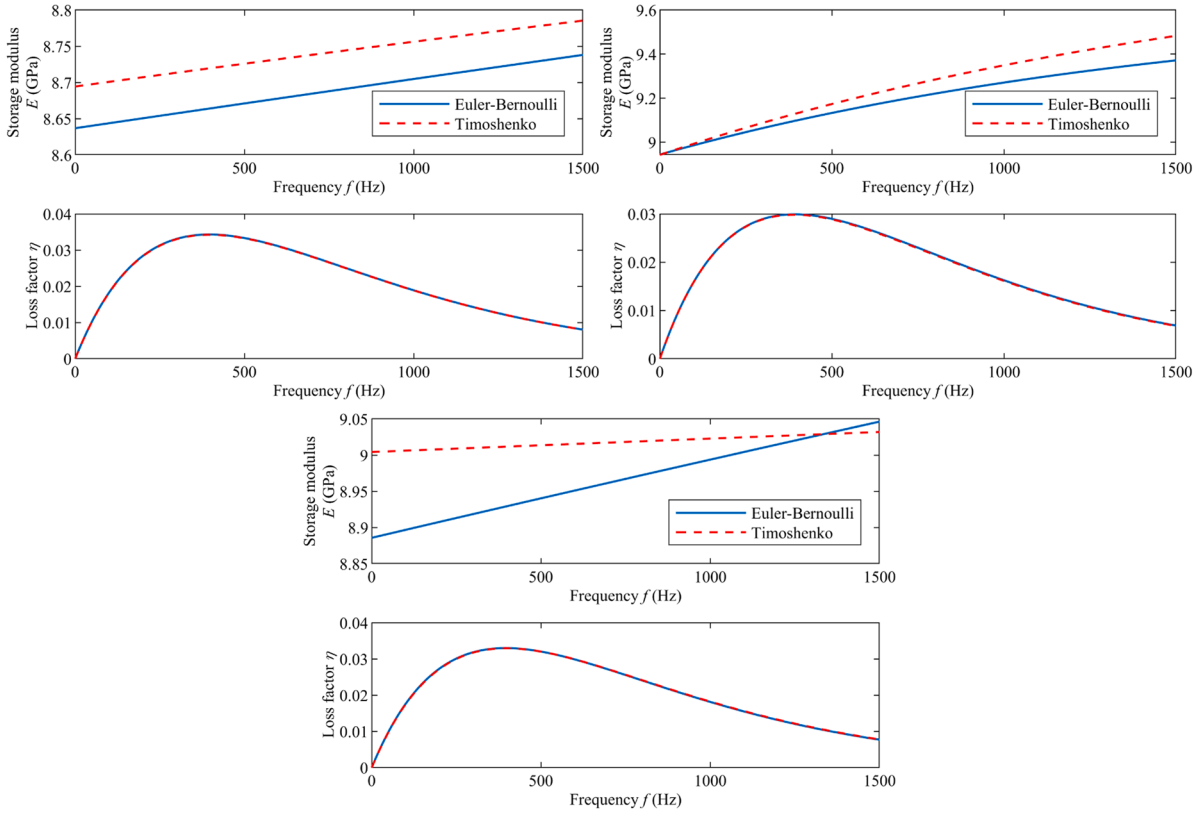

Fig. 6. Frequency-dependent dynamic properties, E^*, of GFRTP specimen groups G1 (top-left), G2 (top-right), and G3 (bottom), identified through the proposed phenomenological model. Each panel contains two subplots: the upper plot displays the storage modulus (E') and the lower plot displays the loss factor (η). The solid blue lines represent the identified properties using the Euler-Bernoulli (EB) beam theory, while the dashed red lines correspond to the Timoshenko beam theory. (For interpretation of the references to colour in this figure legend, the reader is referred to the web version of this article.)

Table 6
Percentage errors in frequency, amplitude, and damping ratio of the numerical transmissibility, T^*, with respect to the experimental data, T^*_{exp}.

	FEM	Mode 1			Mode 2		
		$\epsilon_{f,1}$	$\epsilon_{A,1}$	$\epsilon_{\eta,1}$	$\epsilon_{f,2}$	$\epsilon_{A,2}$	$\epsilon_{\eta,2}$
G1	EB	0.00	−7.64	+0.00	−0.05	+2.05	−5.75
	Tim.	+0.57	−7.63	−0.57	−0.05	+1.76	−8.65
G2	EB	+1.14	−7.63	+13.00	0.00	−1.33	+5.17
	Tim.	+1.70	−7.63	+12.37	0.00	−1.59	+5.17
G3	EB	+1.13	−7.64	−1.12	−0.04	−12.23	+11.81
	Tim.	+1.13	−7.63	−1.12	−0.04	−11.84	+11.81

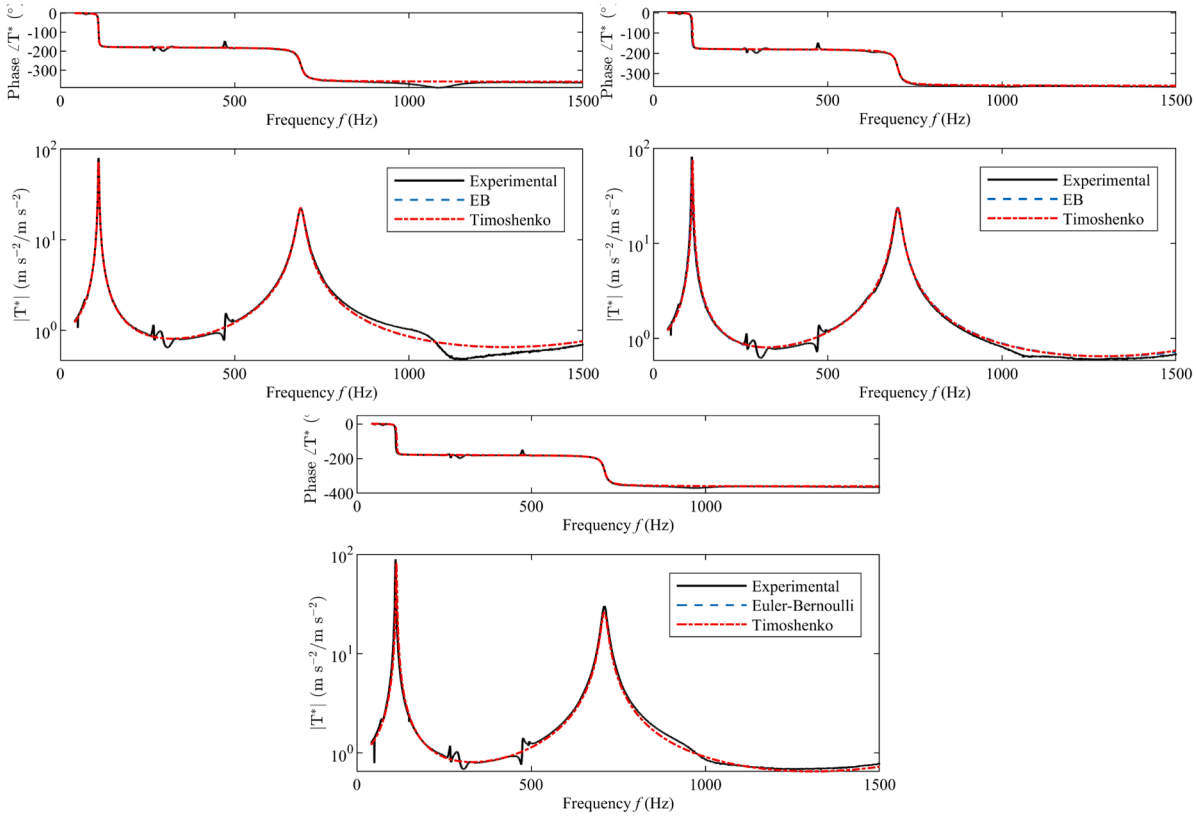

Fig. 7. Frequency-response transmissibility of the GFRTP specimen groups G1 (top left), G2 (top right), and G3 (bottom). The solid black lines represent the experimental data, whereas the dashed blue lines correspond to the fitted Euler-Bernoulli (EB) model and the dash-dotted lines to the fitted Timoshenko model. (For interpretation of the references to colour in this figure legend, the reader is referred to the web version of this article.)

5. Conclusions

This study presents a robust and accurate methodology for the high-frequency dynamic modeling of glass fiber-reinforced thermoplastic GFRTP composites. The main conclusions derived from this work are summarized as follows:

- **Accurate high-frequency characterization via transmissibility:** The proposed experimental-numerical procedure based on seismic transmissibility functions enables the accurate characterization of the complex modulus of GFRTP materials across a broad frequency spectrum (40-1500 Hz). This approach provides a reliable estimation of both the storage modulus and the loss factor, capturing the intrinsic viscoelastic behavior of the composite.
- **Superiority of the phenomenological material model:** The novel phenomenological viscoelastic material model proposed in this study demonstrates significantly higher fidelity than the classical single-branch Maxwell model. By decoupling the storage and loss moduli, the model provides the mathematical flexibility required to independently adjust stiffness dispersion and energy dissipation, thereby reducing modal parameter identification errors. The proposed formulation is therefore well suited for accurately representing the complex modulus within the experimentally characterized frequency range. However, since it does not explicitly enforce the Kramers-Kronig relations, extrapolation of the identified material properties beyond the calibrated frequency bandwidth is not recommended.
- **Versatility and applicability of the FEM framework:** The implemented one-dimensional finite element approach, encompassing both Euler-Bernoulli and Timoshenko theories, represents a highly versatile characterization tool. Beyond its computational efficiency, the primary advantage of this numerical framework lies in its ability to extend the proposed methodology to diverse experimental configurations (such as different boundary conditions or excitation types) where closed-form analytical solutions are not feasible. This flexibility ensures that the characterization remains robust even in complex structural scenarios where traditional analytical benchmarks are unavailable.
- **Robustness of the hybrid optimization strategy:** The combination of the Nelder-Mead simplex algorithm and Particle Swarm Optimization (PSO) ensures a stable and consistent parameter identification process. This hybrid strategy successfully overcomes the non-convex nature of the objective function, providing high repeatability across different GFRTP specimens despite their inherent microstructural heterogeneity.
- **Practical application in automotive design:** Unlike traditional methods such as ASTM E756-05, which rely solely on resonance peaks, this methodology utilizes the entire measured frequency band for curve fitting. This provides a scalable and predictive framework for integrating the dynamic behavior of GFRTP structures into the early stages of the automotive component design process.

CRediT authorship contribution statement

David Miñón: Writing – original draft, Visualization, Software, Methodology, Data curation, Conceptualization; **Jon García-Barruetabeña:** Validation, Supervision, Resources, Project administration, Funding acquisition, Formal analysis, Conceptualization; **Beatriz Achiaga:** Writing – review & editing, Validation, Resources, Project administration, Formal analysis, Conceptualization.

Declaration of generative AI

During the preparation of this work, the authors used ChatGPT to improve the English writing, grammar, and clarity of the manuscript. After using this tool, the authors reviewed and edited the content as needed and take full responsibility for the content of the published article.

Funding

This study received financial support from the Basque Government through the Research Group program IT1507-22 and from the TERCOMAC project (KK-2024/00002).

Replication of results

On behalf of all authors, the corresponding author states that the results presented in the manuscript can be reproduced using the implementation details provided herein.

Declaration of competing interest

The authors declare that they have no known competing financial interests or personal relationships that could have appeared to influence the work reported in this paper.

Data availability

Data will be made available on request.

Appendix A. Finite Element Formulations

The dynamic behavior of the beam is discretized using two-node finite elements. Each node possesses two degrees of freedom (DOFs): transverse displacement w and cross-sectional rotation θ. For an element of length L_e, the nodal displacement vector $\mathbf{u}_e$ is defined as:

$$\mathbf{u}_e(t) = \{w_1,\ \theta_1,\ w_2,\ \theta_2\}^T \tag{A.1}$$

Both Euler-Bernoulli and Timoshenko beam formulations utilize this two-node discretization framework. Rather than reproducing full explicit element mass and complex stiffness matrices-which are standard in finite element literature, this appendix focuses on the exact inclusion of shear deformation and rotary inertia parameters that govern the Timoshenko formulation.

The main distinction between the Euler-Bernoulli theory and the Timoshenko theory lies in the incorporation of transverse shear strain. In the Timoshenko element, the contribution of the shear stiffness is dictated by the non-dimensional shear deformation parameter ϕ, expressed as:

$$\phi = \frac{12E^*(\omega)I}{\kappa GAL_e^2} \tag{A.2}$$

where $E^*(\omega)$ is the dynamic complex Young's modulus of the viscoelastic material, I is the second moment of area of the cross-section, A is the cross-sectional area and L_e is the finite element length. The shear modulus (G) and the shear correction factor (κ) are computed as follows

$$G^* = \frac{E^*}{2(1+\nu)}, \qquad \kappa = \frac{10(1+\nu)}{12+11\nu}. \tag{A.3}$$

The parameter ϕ modifies the Hermitian shape functions to account for additional compliance due to shear. In the limiting condition where shear rigidity approaches infinity ($GA \to \infty$), the shear parameter collapses to zero ($\phi \to 0$). Under this condition, cross-sectional rotations match the slope of the neutral axis ($\theta = \partial w/\partial x$), and the Timoshenko $\mathbf{K_e}$ and $\mathbf{M_e}$ element matrices reduce identically to those of the classical Euler-Bernoulli element.

For heterogeneous structures such as GFRTP, the effective isotropic elastic properties depend on the constituent phases. The equivalent Poisson's ratio ν of the GFRTP composite is estimated via the linear Voigt rule of mixtures:

$$\nu = V_f \nu_f + V_m \nu_m \tag{A.4}$$

where $V_f = 0.34$ and $V_m = 0.66$ denote the volume fractions of the E-glass fibers and PP matrix, respectively, while $\nu_f = 0.22$ and $\nu_m = 0.38$ represent their corresponding Poisson's ratios. Evaluating Eq. (A.4) yields an effective Poisson's ratio of $\nu \approx 0.33$.

To account for the non-uniform distribution of transverse shear stress across the rectangular cross-section of the beam, Cowper's shear correction factor κ for a solid rectangular section is evaluated as [48]:

$$\kappa = \frac{10(1+\nu)}{12+11\nu} \approx 0.849 \tag{A.5}$$

References

[1] S. Gharde, B. Kandasubramanian, Mechanothermal and chemical recycling methodologies for the fibre reinforced plastic (FRP), Environ. Technol. Innov. 14 (2019). https://doi.org/10.1016/j.eti.2019.01.005
[2] A. Akbar, K.M. Liew, Assessing recycling potential of carbon fiber reinforced plastic waste in production of eco-efficient cement-based materials, J. Clean. Prod. 274 (2020). https://doi.org/10.1016/j.jclepro.2020.123001
[3] J. Spasenović, I. Blagojević, Composite materials in automotive industry: a review, Industrija 49 (2021). https://doi.org/10.5937/industrija49-34540
[4] B. Ravishankar, S.K. Nayak, M.A. Kader, Hybrid composites for automotive applications - a review, J. Reinf. Plast. Compos. 38 (2019). https://doi.org/10.1177/0731684419849708
[5] J.A. Butenegro, M. Bahrami, Y. Swolfs, J. Ivens, M. Martínez, J. Abenojar, Novel thermoplastic composites strengthened with carbon fiber-reinforced epoxy composite waste rods: development and characterization, Polymers 14 (2022). https://doi.org/10.3390/polym14193951
[6] S. Wen, F. Deng, C. Su, X. Liu, J. Wang, Y. Wang, Addressing aerodynamic noise in vehicles: a hybrid method for noise reduction and signal preservation, Appl. Acoust. 236 (2025) 110747. https://doi.org/10.1016/j.apacoust.2025.110747
[7] J. Zhang, V.S. Chevali, H. Wang, C.H. Wang, Current status of carbon fibre and carbon fibre composites recycling, Compos. B: Eng. 193 (2020). https://doi.org/10.1016/j.compositesb.2020.108053
[8] V. Shanmugam, O. Das, R.E. Neisiany, K. Babu, S. Singh, M.S. Hedenqvist, F. Berto, S. Ramakrishna, Polymer recycling in additive manufacturing: an opportunity for the circular economy, Mater. Circ. Econ. 2 (2020). https://doi.org/10.1007/s42824-020-00012-0
[9] X. Zhao, K. Copenhaver, L. Wang, M. Korey, D.J. Gardner, K. Li, M.E. Lamm, V. Kishore, S. Bhagia, M. Tajvidi, H. Tekinalp, O. Oyedeji, S. Wasti, E. Webb, A.J. Ragauskas, H. Zhu, W.H. Peter, S. Ozcan, Recycling of natural fiber composites: challenges and opportunities, Resour. Conserv. Recycl. 177 (2022). https://doi.org/10.1016/j.resconrec.2021.105962
[10] E. Morici, N.T. Dintcheva, Recycling of thermoset materials and thermoset-based composites: challenge and opportunity, Polymers 14 (2022). https://doi.org/10.3390/polym14194153
[11] I.O. Oladele, C.J. Okoro, A.S. Taiwo, L.N. Onuh, N.I. Agbeboh, O.P. Balogun, P.A. Olubambi, S.S. Lephuthing, Modern trends in recycling waste thermoplastics and their prospective applications: a review, J. Compos. Sci. 7 (2023). https://doi.org/10.3390/jcs7050198
[12] M. Overcash, J. Twomey, E. Asmatulu, E. Vozzola, E. Griffing, Thermoset composite recycling - driving forces, development, and evolution of new opportunities, J. Compos. Mater. 52 (2018). https://doi.org/10.1177/0021998317720000
[13] S.K. Gopalraj, T. Kärki, A review on the recycling of waste carbon fibre/glass fibre-reinforced composites: fibre recovery, properties and life-cycle analysis, SN Appl. Sci. 2 (2020). https://doi.org/10.1007/s42452-020-2195-4
[14] X. Xue, S.Y. Liu, Z.Y. Zhang, Q.Z. Wang, C.Z. Xiao, A technology review of recycling methods for fiber-reinforced thermosets, J. Reinf. Plast. Compos. 41 (2022) 459–480. https://doi.org/10.1177/07316844211055208
[15] R. Bernatas, S. Dagreou, A. Despax-Ferreres, A. Barasinski, Recycling of fiber reinforced composites with a focus on thermoplastic composites, Clean. Eng. Technol. 5 (2021). https://doi.org/10.1016/j.clet.2021.100272
[16] Y.S. Türker, F. Öztürk, Y. Öz, Review of recycling methods of thermoplastic composite materials, Polym.-Plast. Technol. Mater. 63 (2024) 1693–1713. https://doi.org/10.1080/25740881.2024.2352148
[17] D.J. Kwon, N.S.R. Kim, Y.J. Jang, H.H. Choi, K. Kim, G.H. Kim, J. Kong, S.Y. Nam, Impacts of thermoplastics content on mechanical properties of continuous fiber-reinforced thermoplastic composites, Compos. B: Eng. 216 (2021). https://doi.org/10.1016/j.compositesb.2021.108859
[18] B.M. Scheuring, N. Christ, J. Blarr, W.V. Liebig, J. Hohe, J. Montesano, K.A. Weidenmann, Experimental and homogenized orientation-dependent properties of hybrid long fiber-reinforced thermoplastics, Int. J. Mech. Sci. 280 (2024). https://doi.org/10.1016/j.ijmecsci.2024.109470

[19] P. Bajurko, Comparison of damage resistance of thermoplastic and thermoset carbon fibre-reinforced composites, J. Thermoplast. Compos. Mater. 34 (2021) 303–315. https://doi.org/10.1177/0892705719844550
[20] K. Abedi, H. Seraj, R. Ansari, M.K. Hassanzadeh-Aghdam, J. Jamali, S. Sahmani, A micromechanics-based numerical study on the viscoelastic damping in carbon nanotube/polymer nanocomposites, Compos. Sci. Technol. 274 (2026) 111449. https://doi.org/10.1016/j.compscitech.2025.111449
[21] K. Abedi, H. Seraj, R. Ansari, M.K. Hassanzadeh-Aghdam, J. Jamali, Micromechanics-based finite element modeling of damping in hollow spheres/fiber-reinforced polymer composites, J. Thermoplast. Compos. Mater. 39 (5) (2026) 2230–2248. https://doi.org/10.1177/08927057251388608
[22] N. Saba, M. Jawaid, O.Y. Alothman, M.T. Paridah, A review on dynamic mechanical properties of natural fibre reinforced polymer composites, Constr. Build. Mater. 106 (2016). https://doi.org/10.1016/j.conbuildmat.2015.12.075
[23] J. Schalnat, D.G. Gómez, L. Daelemans, I. De Baere, K. De Clerck, W.V. Paepegem, Influencing parameters on measurement accuracy in dynamic mechanical analysis of thermoplastic polymers and their composites, Polym. Test. 91 (2020). https://doi.org/10.1016/j.polymertesting.2020.106799
[24] J. Feng, Z. Guo, Temperature-frequency-dependent mechanical properties model of epoxy resin and its composites, Compos. B: Eng. 85 (2016). https://doi.org/10.1016/j.compositesb.2015.09.040
[25] V. Dorléans, R. Delille, D. Notta-Cuvier, F. Lauro, E. Michau, Time-temperature superposition in viscoelasticity and viscoplasticity for thermoplastics, Polym. Test. 101 (2021). https://doi.org/10.1016/j.polymertesting.2021.107287
[26] E.M. Kerwin, Damping of flexural waves by a constrained viscoelastic layer, J. Acoust. Soc. Am. 31 (1959). https://doi.org/10.1121/1.1907821
[27] E.E. Ungar, E.M. Kerwin, Loss factors of viscoelastic systems in terms of energy concepts, J. Acoust. Soc. Am. 34 (1962). https://doi.org/10.1121/1.1918227
[28] V. Sessner, W. Liebig, A. Jackstadt, D. Schmid, T. Ehrig, K. Holeczek, N. Graebner, P. Kostka, U. Wagner, K. Weidenmann, L. Kärger, Wide scale characterization and modeling of the vibration and damping behavior of CFRP-elastomer-metal laminates-comparison and discussion of different test setups, Appl. Compos. Mater. 28 (2021) 1715–1746. https://doi.org/10.1007/s10443-021-09934-7
[29] J. García-Barruetabeña, D. Miñón, B. Achiaga, F. Cortés, Characterization of the dynamic properties of an automotive laminated glass ceiling, Bol. Soc. Esp. Cerám. Vidrio (2024). https://doi.org/10.1016/j.bsecv.2024.05.001
[30] F. Cortés, M.J. Elejabarrieta, Viscoelastic materials characterisation using the seismic response, Mater. Des. 28 (2007) 2054–2062. https://doi.org/10.1016/j.matdes.2006.05.032
[31] R. Xiao, H. Sun, W. Chen, An equivalence between generalized Maxwell model and fractional Zener model, Mech. Mater. 100 (2016) 148–153.
[32] S.M. Han, H. Benaroya, T. Wei, Dynamics of transversely vibrating beams using four engineering theories, J. Sound Vib. 225 (5) (1999) 935–988.
[33] S.P. Timoshenko, LXVI. On the correction for shear of the differential equation for transverse vibrations of prismatic bars, Lond. Edinb. Dublin Philos. Mag. J. Sci. 41 (245) (1921) 744–746. https://doi.org/10.1080/14786442108636264
[34] D.L. Thomas, J.M. Wilson, R.R. Wilson, Timoshenko beam finite elements, J. Sound Vib. 31 (3) (1973) 315–330. https://doi.org/10.1016/S0022-460X(73)80276-7
[35] J.A. Nelder, R. Mead, A simplex method for function minimization, Comput. J. 7 (1965) 308–313. https://doi.org/10.1093/comjnl/7.4.308
[36] M.A. Luersen, R.L. Riche, Globalized nelder-mead method for engineering optimization, in: Computers and Structures, vol. 82, 2004. https://doi.org/10.1016/j.compstruc.2004.03.072
[37] S. Takenaga, Y. Ozaki, M. Onishi, Practical initialization of the Nelder-Mead method for computationally expensive optimization problems, Optim. Lett. 17 (2023). https://doi.org/10.1007/s11590-022-01953-y
[38] P.C. Wang, T.E. Shoup, Parameter sensitivity study of the Nelder-Mead simplex method, Adv. Eng. Softw. 42 (2011). https://doi.org/10.1016/j.advengsoft.2011.04.004
[39] F. Gao, L. Han, Implementing the Nelder-Mead simplex algorithm with adaptive parameters, Comput. Optim. Appl. 51 (2012). https://doi.org/10.1007/s10589-010-9329-3
[40] R. Eberhart, J. Kennedy, New optimizer using particle swarm theory, in: Proceedings of the International Symposium on Micro Machine and Human Science, 1995. https://doi.org/10.1109/mhs.1995.494215
[41] J. Kennedy, R. Eberhart, Particle swarm optimization, in: Proceedings of ICNN'95-International Conference on Neural Networks, vol. 4, IEEE, 1995, pp. 1942–1948.
[42] S.K.S. Fan, Y.C. Liang, E. Zahara, Hybrid simplex search and particle swarm optimization for the global optimization of multimodal functions, Eng. Optim. 36 (2004). https://doi.org/10.1080/0305215041000168521
[43] E. Zahara, Y.T. Kao, Hybrid Nelder-Mead simplex search and particle swarm optimization for constrained engineering design problems, Expert Syst. Appl. 36 (2009). https://doi.org/10.1016/j.eswa.2008.02.039
[44] B.R. Hauser, B.P. Wang, Design optimization of a rotordynamic beam system with elastic supports to minimize flexural responses using a combined optimization algorithm, Struct. Multidiscip. Optim. 61 (2020) 2037–2055. https://doi.org/10.1007/s00158-019-02452-y
[45] F. Cortés, M.J. Elejabarrieta, Modelling viscoelastic materials whose storage modulus is constant with frequency, Int. J. Solids Struct. 43 (2006) 7721–7726. https://doi.org/10.1016/j.ijsolstr.2006.03.022
[46] R. De L. Kronig, On the theory of dispersion of X-rays, J. Opt. Soc. Am. 12 (6) (1926) 547–557.
[47] T. Pritz, Unbounded complex modulus of viscoelastic materials and the Kramers-Kronig relations, J. Sound Vib. - J Sound Vib. 279 (2005) 687–697. https://doi.org/10.1016/j.jsv.2003.11.040
[48] G. Cowper, The shear coefficient in Timoshenko's beam theory, J. Appl. Mech. 33 (1966) 335–340. https://doi.org/10.1115/1.3625046